

Conf-9506126--2

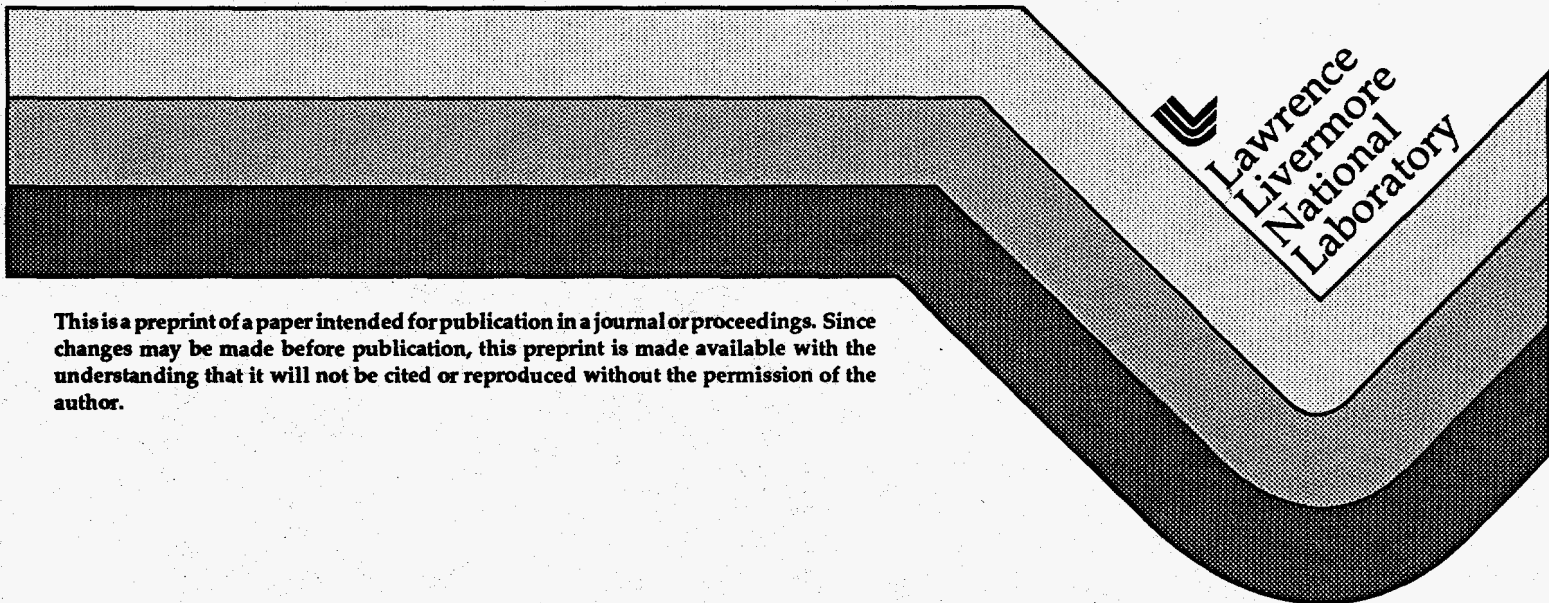
UCRL-JC-120546
PREPRINT

Mapping Hidden Aircraft Defects with Dual-Band Infrared Computed Tomography

N. K. Del Grande
P. F. Durbin

This paper was prepared for submittal to the
SPIE Nondestructive Evaluation of Aging Aircraft Airports,
Aerospace Hardware & Materials
Oakland, California
June 6-8, 1995

April 3, 1995



This is a preprint of a paper intended for publication in a journal or proceedings. Since changes may be made before publication, this preprint is made available with the understanding that it will not be cited or reproduced without the permission of the author.

DISCLAIMER

This document was prepared as an account of work sponsored by an agency of the United States Government. Neither the United States Government nor the University of California nor any of their employees, makes any warranty, express or implied, or assumes any legal liability or responsibility for the accuracy, completeness, or usefulness of any information, apparatus, product, or process disclosed, or represents that its use would not infringe privately owned rights. Reference herein to any specific commercial products, process, or service by trade name, trademark, manufacturer, or otherwise, does not necessarily constitute or imply its endorsement, recommendation, or favoring by the United States Government or the University of California. The views and opinions of authors expressed herein do not necessarily state or reflect those of the United States Government or the University of California, and shall not be used for advertising or product endorsement purposes.

DISCLAIMER

Portions of this document may be illegible in electronic image products. Images are produced from the best available original document.

Mapping hidden aircraft defects with dual-band infrared computed tomography

Nancy K. Del Grande and Philip F. Durbin
Lawrence Livermore National Laboratory,
P.O. Box 808, Livermore CA 94551

ABSTRACT

Infrared computed tomography (IRCT) is a promising, non-contact, nondestructive evaluation tool used to inspect the mechanical integrity of large structures. We describe on-site, proof-of-principle demonstrations of IRCT to inspect defective metallic and composite structures. The IRCT system captures time sequences of heat-stimulated, dual-band infrared (DBIR) thermal maps for flash-heated and naturally-heated targets. Our VIEW algorithms produce co-registered thermal, thermal inertia, and thermal-timegram maps from which we quantify the percent metal-loss corrosion damage for airframes and the defect sites, depths, and host-material physical properties for composite structures. The IRCT method clarifies the type of defect, e.g., corrosion, fabrication, foreign-material insert, delamination, unbond, void, and quantifies the amount of damage from the defect, e.g., the percent metal-loss from corrosion in metal structures, the depth, thickness, and areal extent of heat damage in multi-layered composite materials. Potential long-term benefits of IRCT technology are in-service monitoring of incipient corrosion damage, to avoid catastrophic failure and production-monitoring of cure states for composite materials.

1. INTRODUCTION

1.1 Conventional single-band infrared (SBIR) thermography

Recent applications of thermography include nondestructive inspections (NDI) of airframes, composites, and aerospace structures. Infrared imaging and detection has the potential of rapidly inspecting large areas at video frame rates (30 frames per second) to provide an early warning of subsurface defects, e.g., corrosion thinning, sites with poor adhesive bonding (unbonds), voids, inserts, and delaminations.

Using single-band infrared (SBIR) imaging methods, scientists have successfully depicted the sites of subsurface defects in manmade structures.¹⁻⁵ However, the exact amount of structural damage caused by these subsurface defects alludes detection. More uniform pulsed heat sources, more sensitive temperature-sensing methods, higher temporal resolution, faster image-data capture, and algorithms which remove reflected IR backgrounds are needed to identify weak heat flows at the sites of deep structural defects.

1.2 Motivation to improve conventional thermography

Conventional SBIR imaging does not distinguish between major defects that affect the mechanical integrity of large structures, e.g., more than 10% corrosion thickness reduction, and minor defects that do not warrant costly repairs, e.g., ripples, sealant globs, uneven paint, stains, tape markers, scratches, dents, and insulation wads attached to the interior of the aircraft fuselage. A recent round-robin investigation of commercial NDI equipment used to detect hidden corrosion on U.S. Air Force aircraft indicated that false detection of corrosion results in unnecessary and destructive exploratory maintenance.⁶

Currently, safety regulations require major expenditures of time and monies to provide assurance of aircraft reliability and pipeline integrity. Yet with aging, exposure, and use, airframes and pipelines corrode, and advanced composite structures which do not corrode are subject to heat and impact damage. Our focus at LLNL has been to to avoid costly, unnecessary, and destructive exploratory maintenance by developing a fast, reliable, nonintrusive, inspection method to quantify the amount of corrosion-thinning in metal structures, and the volume of heat- damage in composite structures.

To this end, we have: (1) instigated thermography equipment improvements; (2) developed software algorithms for more reliable and quantitative temperature measurements; (3) imaged the subtle heat flow signatures associated with deep structural defects; and (4) removed false-defect signatures. The application of thermography as a quantitative, NDI, thermal imaging tool, has significant potential to improve the safety, reliability and affordability of airframes and pipelines. Once the technology we have developed is transferred to the thermography equipment manufacturers and inspection services communities, it is expected to provide cost savings advantages for the transportation, petrochemical and aerospace industries.

1.3 Dynamic, emissivity-corrected, dual-band infrared thermography

The Lawrence Livermore National Laboratory has pioneered applications of dynamic, emissivity-corrected, dual-band infrared (DBIR) thermography. ⁷⁻¹⁵ This method quantifies corrosion, e.g., percent metal-loss, within flash-heated airframes, by mapping subtle heat flows from deep structural defects. Compared to SBIR methods, the DBIR methods provide from five-to-ten-times improved signal-to-noise ratios, and better interpretability of subtle heat flow anomalies from deep structural defects. Improved temperature contrast, clutter removal, and quantification of material losses, are features of the DBIR methods that clarify interpretation of defect sites and classify defect types.

1.4 DBIR high contrast temperature and emissivity-noise maps

Using DBIR image ratios, e.g., from DBIR cameras which scan flash-heated targets at infrared wavelengths of 3-5 μm and 8-12 μm , we enhance surface temperature contrast. Also, we remove the mask of surface emissivity clutter, e.g., from dirt, dents, markings, tape, sealants, uneven paint, paint stripper, exposed metal and roughness variations. This clarifies interpretation of subtle heat flow anomalies associated with hidden defects and corrosion. We compute DBIR image ratios of high-contrast temperature (T^5), and emissivity-noise (E-ratio) maps, based on an expansion of Planck's radiation law, ¹⁶ which we have applied successfully for several different applications: ¹⁷⁻²²

The results of the expansion are:

$$I_{\lambda} = e_{\lambda} T^{50/\lambda} \quad (1)$$

where I_{λ} is the intensity at a given wavelength, e_{λ} is the emissivity at that wavelength, T is the absolute temperature in Kelvin and λ is the wavelength in micrometers. We can obtain high-contrast normalized temperature maps by computing DBIR image ratios for a greybody surface where $e_5 = e_{10}$:

$$\frac{I_5}{I_{10}} = \frac{e_5 T^{50/5}}{e_{10} T^{50/10}} = \frac{e_5}{e_{10}} T^5 \quad \text{and} \quad (T/T_{av})^5 = (SW/SW_{av}) / (LW/LW_{av}) \quad (2)$$

We can obtain normalized emissivity-noise maps by computing the DBIR emissivity ratios to contrast non-greybody features:

$$\frac{(I_{10})^2}{I_5} = \frac{(e_{10})^2 (T^5)^2}{e_5 T^{10}} = \frac{(e_{10})^2}{e_5} \quad \text{and} \quad \text{E-ratio} = (LW/LW_{av})^2 / (SW/SW_{av}) \quad (3)$$

where SW is the short-wavelength intensity (e.g., I_5), SW_{av} is the average value of the pixels in SW , LW is the long wavelength intensity (e.g., I_{10}) and LW_{av} is the average value of the pixels in LW .

1.5 Thermal inertia mapping for airframe corrosion damage detection

We developed thermal inertia maps, which have been used previously for other applications, ^{23,24} by solving the heat transfer equation for a thick panel with an instantaneous surface heat flux: ²⁵

$$T(x,t) = \frac{q}{\sqrt{4\pi k\rho c t}} \exp\left(-\frac{x^2}{4\alpha t}\right) \quad (4)$$

where T is temperature, x is the distance from the surface, k is thermal conductivity, ρ is density, c is heat capacity, α is thermal diffusivity, t is time and q is the surface heat flux. For a semi-infinite solid approximation, the surface temperature is proportional to the inverse square root of time. In practice, we map the target composite thermal inertia, $(k\rho c)^{1/2}$, based on the inverse slope of the surface temperature versus the inverse square root of time. Thermal inertia maps characterize the bulk thermal properties of metal and multi-layered composite structures. Composite thermal inertia maps characterize shallow target defects at early times and deeper target defects at late times. They depict the depth of corrosion-related thickness losses in metal targets and the defect type, e.g., implant, void, or delamination, and depth in multi-layered composite structures.

2. MAPPING HIDDEN AIRCRAFT DEFECTS

2.1 Description of Infrared Computed Tomography (IRCT) system and mapping procedure

During 1994, we developed a field-portable infrared computed tomography (IRCT) system for non-destructive inspection (NDI) of flash-heated and naturally-heated targets. The system has a unique combination of spatial (0.5 mm), thermal (0.05 °C), and temporal (0.5 ms) resolution. It maps co-registered 3 to 5 μm and 8 to 12 μm images. Ratios of these images provide improved thermal precision, definition, and interpretability, which is needed to depict weak heat flow anomalies from deep defects in multi-layered metal and composite structures.

We use a patented infrared computed tomography (IRCT) method with a uniform pulsed heat load. We measure the dynamic temperature, temperature-timegram (cooling rate) and thermal inertia variations, after the arrival of a 4.2 millisecond duration heat flash. Using image ratios for the two infrared wavebands, we create both enhanced temperature contrast and emissivity-ratio maps. These maps enhance the surface temperature contrast associated with anomalous heat flows at target defect sites. They improve the signal-to-noise ratios, decrease the effects of non-uniform surface heating, and remove the surface clutter, e.g., uneven paint, dirt, tape marks, and roughness variations, which obscure defect signatures.

The IRCT system reconstructs defect sites and depths in three dimensions from time-sequences of dual-band infrared thermal maps for flash-heated and naturally-heated targets. LLNL/VIEW code algorithms produce coregistered thermal, thermal-inertia, and thermal-timegram (cooling-rate) maps needed to quantify corrosion damage for airframes and to characterize defect sites, types, depths, and host-material physical properties for composite structures. The IRCT method clarifies the type of defect, e.g., corrosion, fabrication, foreign material insert, and quantifies the damage, e.g., percent thickness-loss from corrosion.

2.2 Dynamic thermal maps used for IRCT reconstructions

Using high-contrast temperature, timegram (cooling rate) and thermal inertia maps, (1) we quantified percent metal loss from corrosion; (2) we characterized defect types, sizes, thicknesses and depths; (3) we removed potential false calls produced by surface irregularities, non-uniform heat sources, ripples, patches, sealant globs, and insulation; and (4) we used time-varying sequences of thermal, thermal timegram (cooling-rate) and thermal-inertia profiles, as two-dimensional (2D) time slices (tomograms) for IRCT reconstructions to image target defects in three-dimensional (3D) space.

Calibrated temperature maps measure the percent metal-loss damage from corrosion. Timegram cooling-rate maps, e.g., sequences of time-resolved linescan thermal profiles, measure the dynamic pulsed thermal response of the target material. Thermal inertia maps are needed for infrared computed tomography (IRCT) reconstructions to characterize defects in all three spatial dimensions. Early time thermal inertia maps identify shallow, near-surface irregularities, e.g., paint, rivets, and sealant globs. Late time thermal inertia maps identify deeper, interior and far-surface, irregularities, e.g., corrosion-loss defects, unbonds, and far-surface insulation. Thermal inertia maps image thermal property differences for bulk materials and provide depth information about the host target material and subsurface defects.

2.3 Pulsed thermal analyses characterize target defects without assuming thermal waves

Target defects were characterized by their location, depth and cooling rate signatures which contrasted with their host materials. Algorithms were developed to correct for uneven flashlamp heating and to produce co-registered thermal, emissivity and thermal inertia maps. These maps identified and removed false (corrosion-loss) calls. We used pulsed thermal analyses, since we saw no images to support the assumption made by some thermographers that a 4.2-millisecond pulsed heat source would produce thermal waves. We typically imaged sixty sequential timegram (cooling rate) maps, derived from linescan temperature profiles, at 0 to 4.8 seconds after the peak of the flash. The cooling-rate maps for the approximate thirty metal and composite targets which we studied, had no apparent wavelike behavior.

3. INTERPRETABILITY OF RESULTS

3.1 Corrections to measure heat flows from hidden, subsurface defects

In Figure 1, we used the VIEW image processing code to correct for hot spots from non-uniform pulsed heat sources. We developed correction algorithms for a uniformly-thick (1 mm) aluminum panel and tested them on a known reference standard with gradual thickness variations from about .8 mm, at the center, to 1 mm at the perimeter. The non-uniform heat source produced a 1 °C surface temperature rise for a 13.0 % (uncorrected, at left) and 15.8 % (corrected, at right) thickness reduction. The corrected, compared to the uncorrected, metal-loss per degree Celsius was larger by 22%.

3.2 Corrosion metal-loss defects in airframes

Since we typically do not know the thicknesses of the various layers within most multi-layered targets, it is not always possible to correct for non-uniform heat sources. A uniform pulsed heat source was developed by Bales Scientific Inc. We borrowed this heat source and high-efficiency, high-reflectance hood. This saved us substantial time and monies needed to achieve quantitative, e.g., percent corrosion metal-loss, aircraft corrosion-damage measurements at the FAA/AANC Aging Aircraft Nondestructive Inspection Center at Sandia Laboratories in Albuquerque, New Mexico. With the borrowed equipment, we reduced errors associated with metal-loss calibrations by a factor of ten (e.g., from 20 or 30 percent to 2 or 3 percent, and saved the time associated with applying the non-uniform heat source correction algorithms to obtain quantitative results.

In addition to source-uniformity and emissivity-noise corrections, we must tag and remove, fabrication, repair-site and preparation irregularities (e.g., from sealant globs, production ripples, doublers, patches and insulation pads) which could obscure the sites of major structural defects. Corrections were made using dual-band infrared (DBIR) methods to distinguish metal-loss defects from other target irregularities. Based on the Tinker AFB studies, conventional SBIR thermal imaging methods located about as many false as true corrosion-loss defects.⁶ The IRCT method identifies major structural defect sites and removes minor defect sites which pose no threat to the aircraft structural integrity. This potentially reduces repair costs, e.g., by a factor of two, by eliminating false calls which occur about 50% of the time.

Using the dual-band infrared (DBIR) ratios of Equations 2 and 3, we produced high-contrast temperature maps and emissivity-noise maps. These maps removed reflected IR backgrounds and emissivity noise from surface clutter (tape marks, dirt, uneven paint, stains, roughness variations). Both noise and heat flow signals from subsurface defects appeared on the SBIR apparent temperature maps. After removing the non-uniform heat source effects, and the emissivity-noise, only the heat flow signals, e.g., from shallow to deep subsurface defects, appeared on the corrected, high-contrast, DBIR temperature maps.

3.3 Boeing KC-135 panel temperature, timegram and thermal inertia maps

Figures 2, 3, 4 and 5 apply to a corroded Boeing KC-135 panel obtained from Tinker Air Force Base in Oklahoma. Figure 2 shows the 3 to 5 micron (SW) apparent temperature and timegram, e.g., cooling rate, maps respectively at the top, left and the top, right. Figure 2 also shows the 8 to 12 micron (LW) apparent temperature and timegram, e.g., cooling rate, maps respectively at the bottom, left and the bottom, right. The SW and LW temperature maps are taken at 0.4 seconds after the flash. The timegram (cooling rate) maps have times increasing from 0 seconds for the top line of the linescan, to .08 seconds for the bottom line of the linescan, after the flash peak temperature. To emphasize small temperature differences, temperature values were off scale on the timegrams at less than .04 s. Note the spot temperatures at defect sites #1 and #2, which are typically warmer than the spot temperatures at normal sites, without defects, e.g., #3.

Figure 3 shows similar thermal patterns for the SW and LW apparent temperature maps, and the high-contrast DBIR temperature map, which differ significantly from the emissivity-noise map. This is to be expected when, as is customary, the panels are painted black. The black paint allows the target to absorb about six times as much heat, compared to the absorbed heat for unpainted (bare-metal) aluminum targets, since bare metal targets are highly reflective.

Figures 4 and 5 trace the dynamic and thermal inertia signatures of shallow excess sealants, e.g., at site #1, and corrosion-loss defects, e.g., at site #2. In Figure 4, at times less than .15 seconds, site #1 is warmer than site #2, and both are warmer than site #3. At times more than .15 seconds, site #2 is warmer than site #1. In Figure 5, early-time thermal inertia maps, at .08 to .3 s after the flash, tag shallow sealant globs within the lap splice (left of center), while late-time thermal inertia maps, at .9 to 1.6 s after the flash, tag deep corrosion, e.g., metal-loss thinning (right of center).

Interpreting airframe bulges as "pillowing" from expansion of corrosion by-products is highly subjective. Visible indicators of surface bulges vary only slightly for different types of material defects (e.g., corrosion by-products, sealant globs, shallow inserts, insulation wads and production ripples). We interpreted the type of material defect with greater objectivity, by measuring the dynamic pulsed-thermal and thermal inertia responses. This improved the precision, definition and interpretability of our defect-type characterizations for the Boeing KC-135 panel shown in Figure 4 and Figure 5.

3.4 Boeing 737 fuselage temperature, thermal inertia and timegram maps

Figures 6 applies to the Boeing 737 testbed for NDI technology maintained by the FAA/AANC, the Aging Aircraft Nondestructive Inspection Validation Center at Sandia in Albuquerque, NM. Figure 6 provides an overview of approximately five feet, from Body Stations 401 to 465 (right to left), of the Boeing 737 Stringer 26R lap splice on the belly of the aircraft. Temperatures at 0.4 s after the flash in (A), thermal inertias in (B) and timegram cooling rates in (C) are compared.

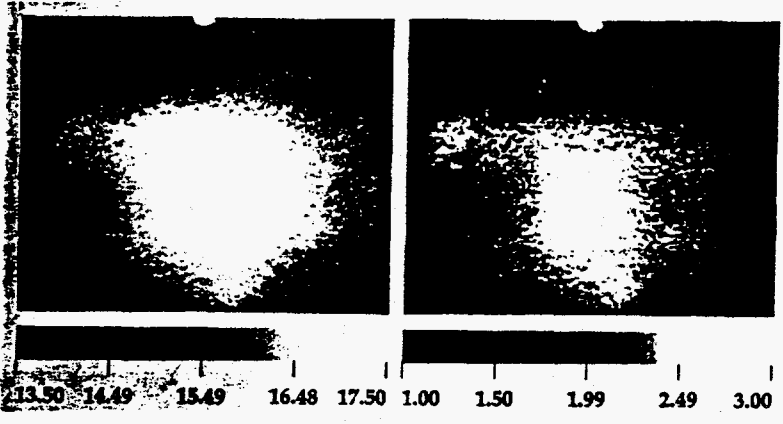


Figure 1

Temperature Maps at 0.4 s (left), Timegrams at 0.04 s (right), SH at top, LH at bottom

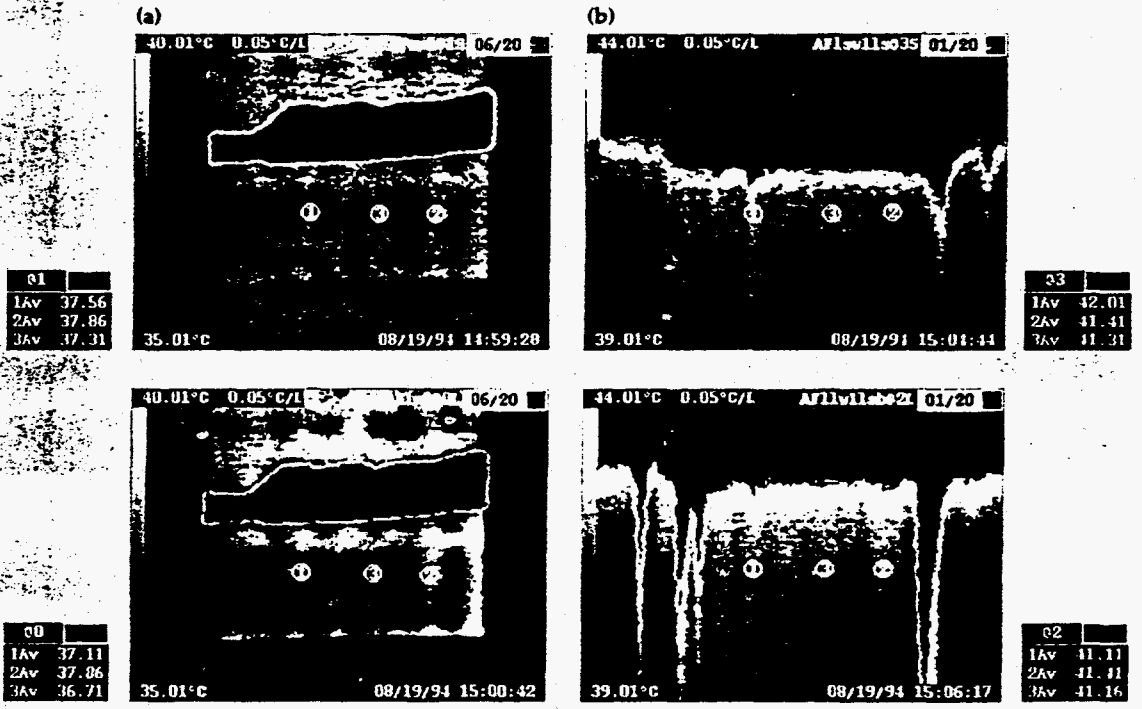


Figure 2

Figure 3.

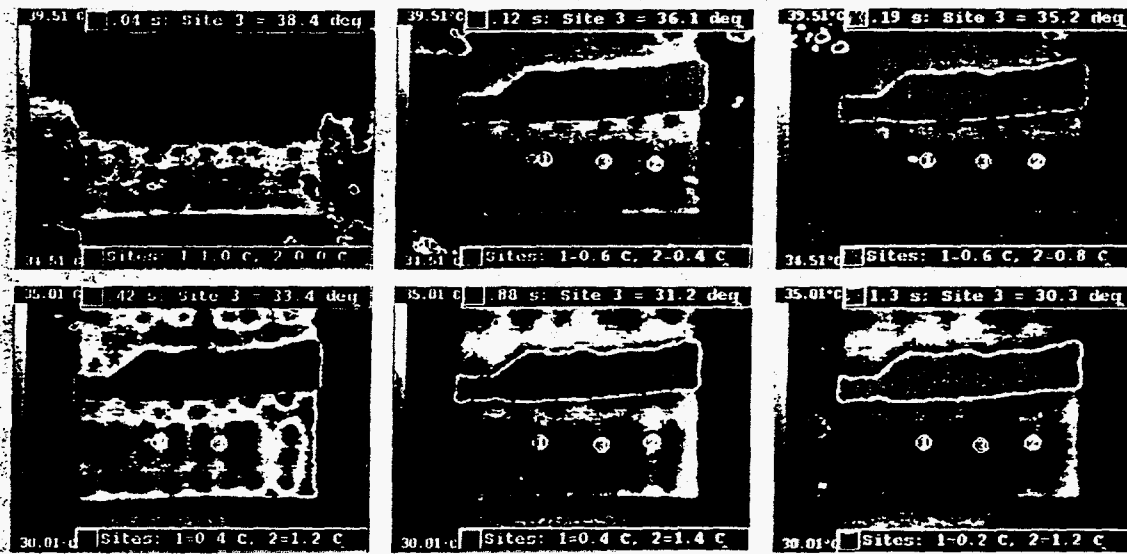
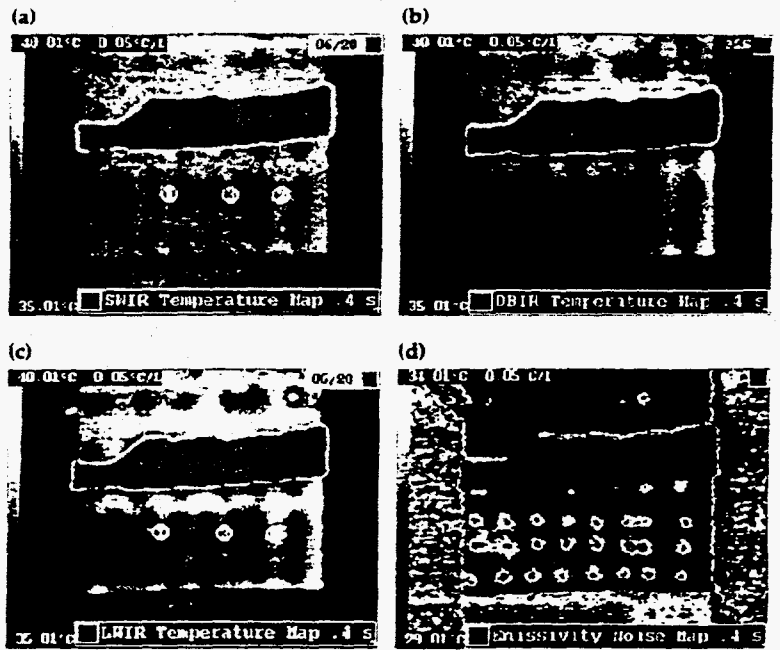
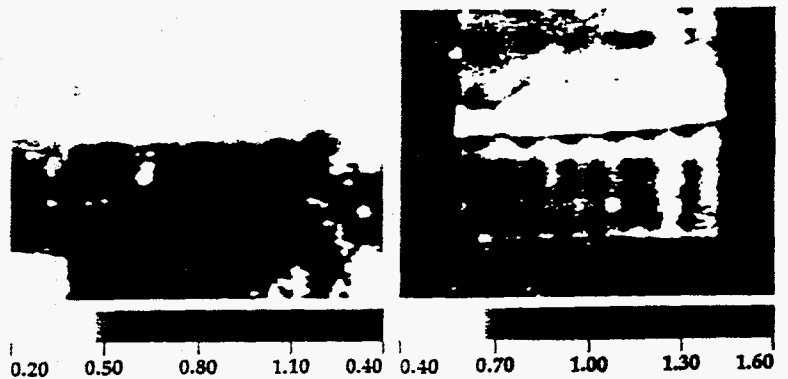
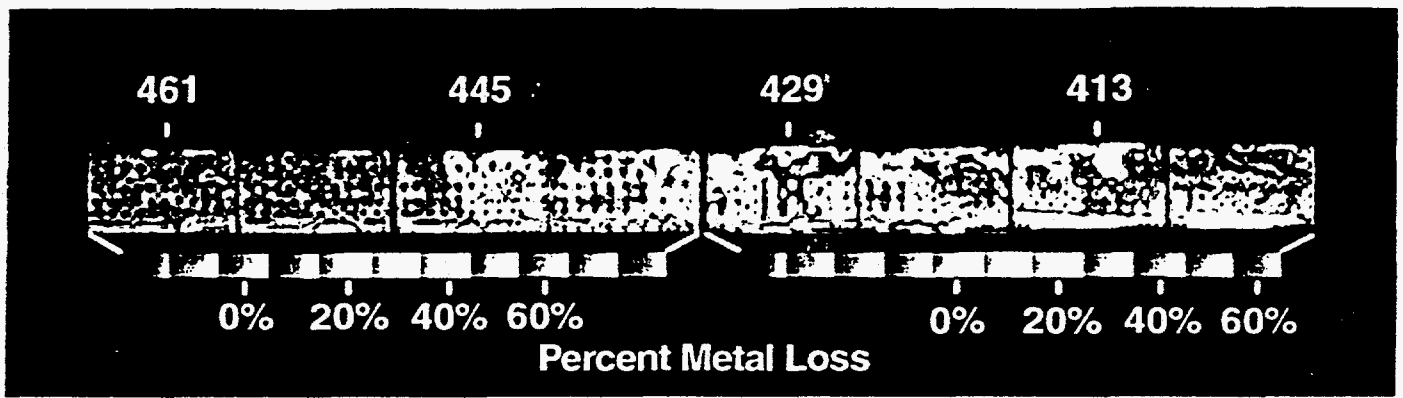


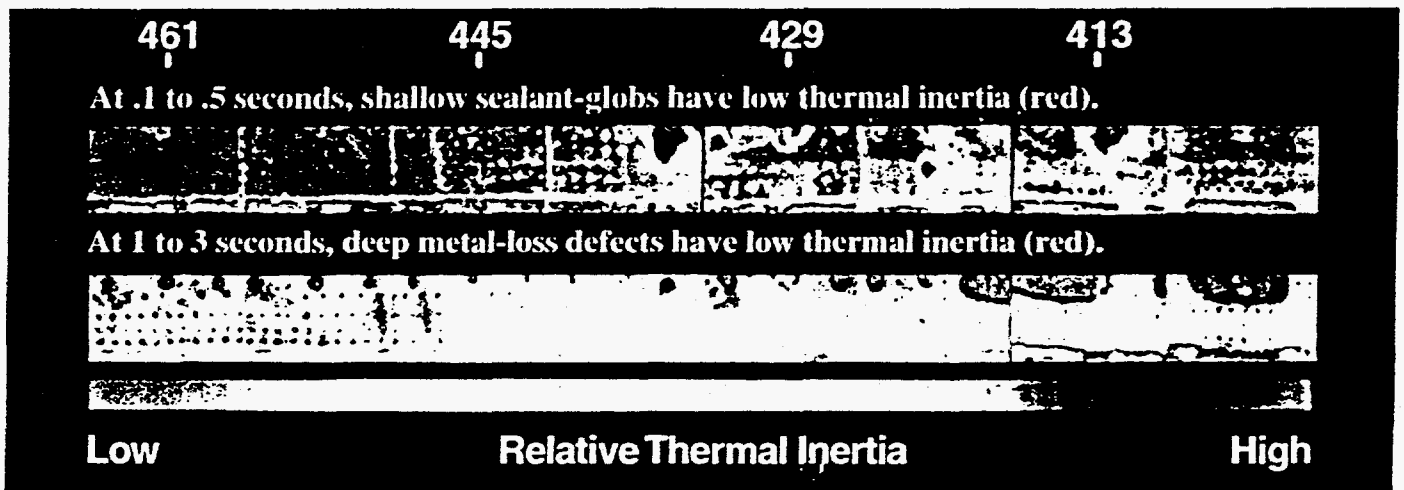
Figure 4.

Figure 5.

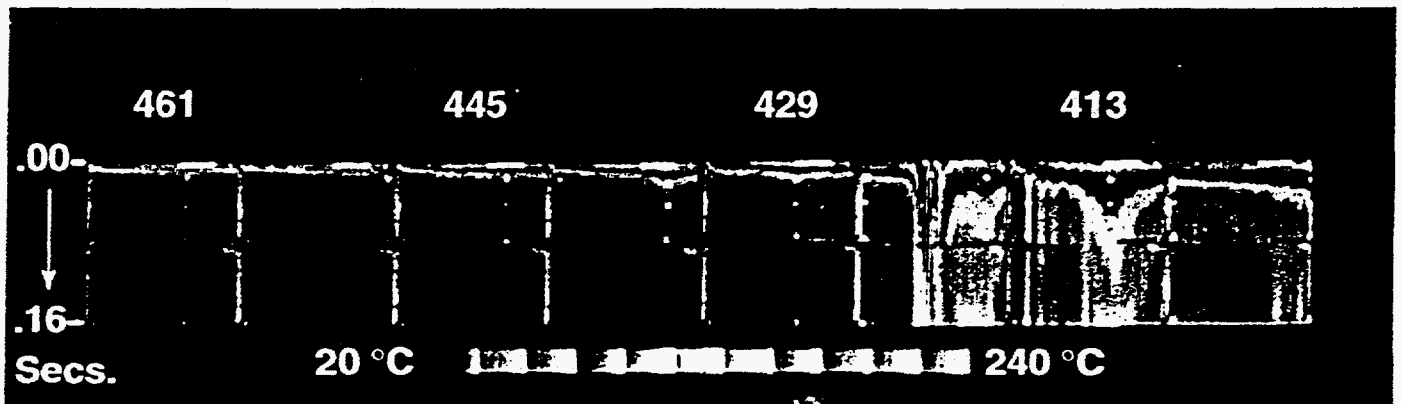




(A) Temperature maps at 0.4 sec. quantify corrosion thickness losses above 5%.



(B) Thermal inertia maps determine defect types and depths.



(C) Timegram cooling rate maps tag lap-splice corrosion damage.

Figure 6. Boeing 737 Stringer 26R Body Stations 401 to 465 (right to left) (A) temperature, (B) thermal inertia and (C) timegram cooling-rate maps.

All three types of thermal maps for the Boeing 737, Stringer 26 section in Figure 6 showed maximum metal loss, e.g., about 50%, near Body Stations BS 401 to BS 421 and minimum metal loss, e.g., less than 5%, near Body Stations BS 449 to BS 465. The panels with the most corrosion appeared (also) to have visible indicators of pillowing from the expansion of corrosion by-products. The corrosion appears to have entered from the interior lap edge, beneath the galley and the latrine. The metal-loss sites in Figure 6 are mostly above and within the lap splice. We analyzed a linescan profile across the lap splice, taken between the first and second row of rivets, from which the timegram cooling rate maps were derived.

The early-time thermal inertia map picked up a patched area with oversized rivets, e.g., at BS 421, and sealant globs above the lap splice, e.g., at BS 435 and BS 413. The late time thermal inertia map tagged smaller low thermal inertia sites, e.g., at BS 435, caused by insulation on the deep interior skin, at the same location as the near-surface sealant globs. We saw evidence of two different fabrication flaws at the same Body Station. The one was at a shallow depth near the exterior skin surface, and the other was at a deeper depth near the interior skin surface.

3.5 Boeing 737 fuselage metal-loss and composite-patch calibration procedures

Figure 7 (A) shows the procedure used for the FAA/AANC Boeing 737 Testbed percent metal loss calibrations. These calibrations were made using the known-thickness Rockwell reference standard. We used the same procedure, calibration geometry and uniform flashlamp heat source, and hood, to calibrate the Rockwell reference standard as we used to measure the thickness loss from corrosion within the lap splice of the Boeing 737. We compared the aircraft metal-loss pulsed thermal signal data for BS 890, S23R, taken with infra-red imaging by LLNL, with the signal data for the same site taken with ultrasound imaging by Iowa State. There was good qualitative agreement.

Figure 7 (B) characterized defects within the B 737 boron-epoxy patch at S23L, Body Station 787. The combined use of ultrasensitive temperature-difference measurements at 0.4 seconds after the flash, with early-time, e.g., 0.8 second, and late-time, e.g., 2.5 second, thermal inertia maps measured relative flaw sizes, types and depths. The circled implant sizes increased from left to right and were nearest the outer-surface at the bottom, and deeper within the patch at the top. The voids along the patch perimeter had four different volumetric sizes. The deep, unbonded sites with air gaps above structural rivets beneath the boron-epoxy patch were best seen on the late-time thermal inertia maps.

3.6 Corrosion thickness-loss calibrations for a F-15 wing box

In Figure 8, corrosion thickness reductions are the dominant signature at the center of SW (top) and LW (bottom) pulsed-thermal DBIR images on the left and thermal timegrams on the right. The timegram cooling-rate maps show time increasing downward on the vertical scale, from 0 to 87 milliseconds. The deep corrosion pit sites, left of center, cool more slowly than their surroundings, except for the thick walls which separate the wing-box channels. The corrosion thickness reductions were measured with the appropriate caliper scale to establish a correlation between the percent metal-loss resulting from corrosion thinning and pitting, and the surface temperature rise at about 50 milliseconds after the heat flash.

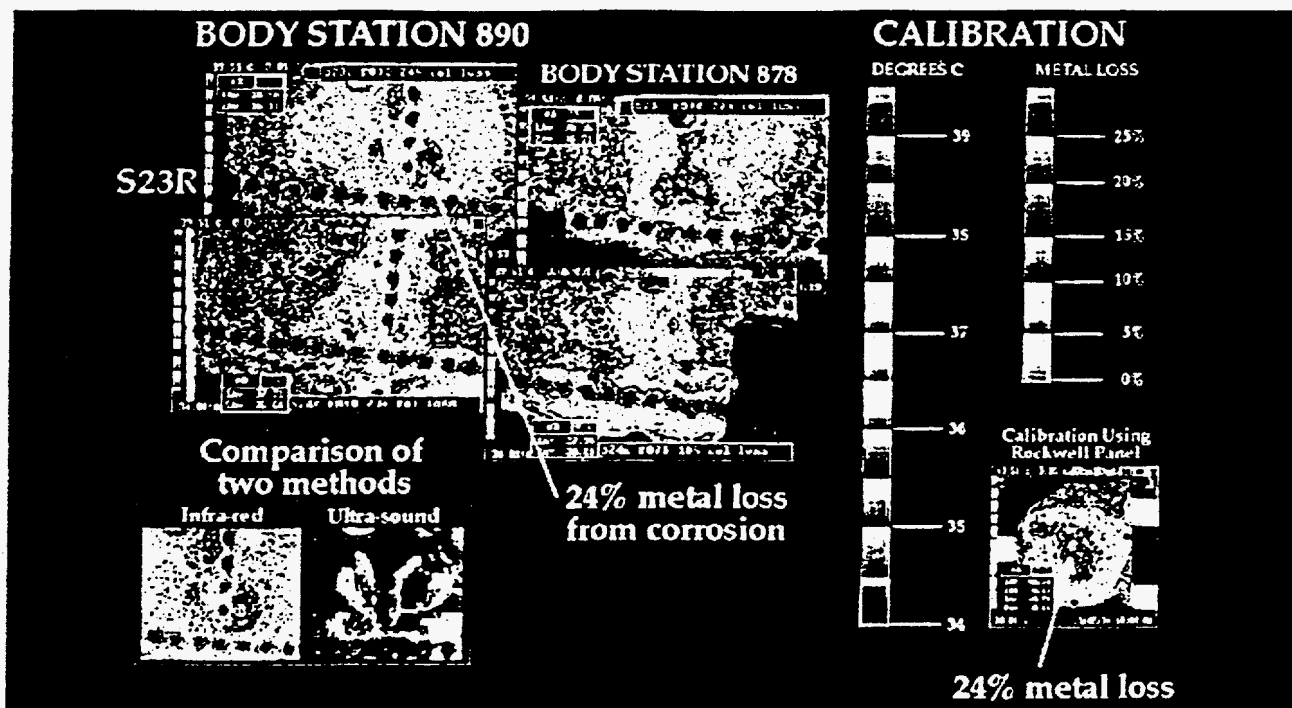
3.7 Imaging and detecting interior-wall corrosion within a quarter-inch steel pipe

We show a deep, oval-shaped, corrosion pit which characterized the inside of a quarter-inch steel pipe provided by Dow Chemical. The early-time, e.g., less than 20 ms, thermal and temporal signatures distinguished the larger-sized corrosion pit from the smaller-sized spots from surface rust seen in Figure 9. The deep corrosion site was more than 50 °C warmer than the surrounding pipe temperatures at less than 20 ms after the flash.

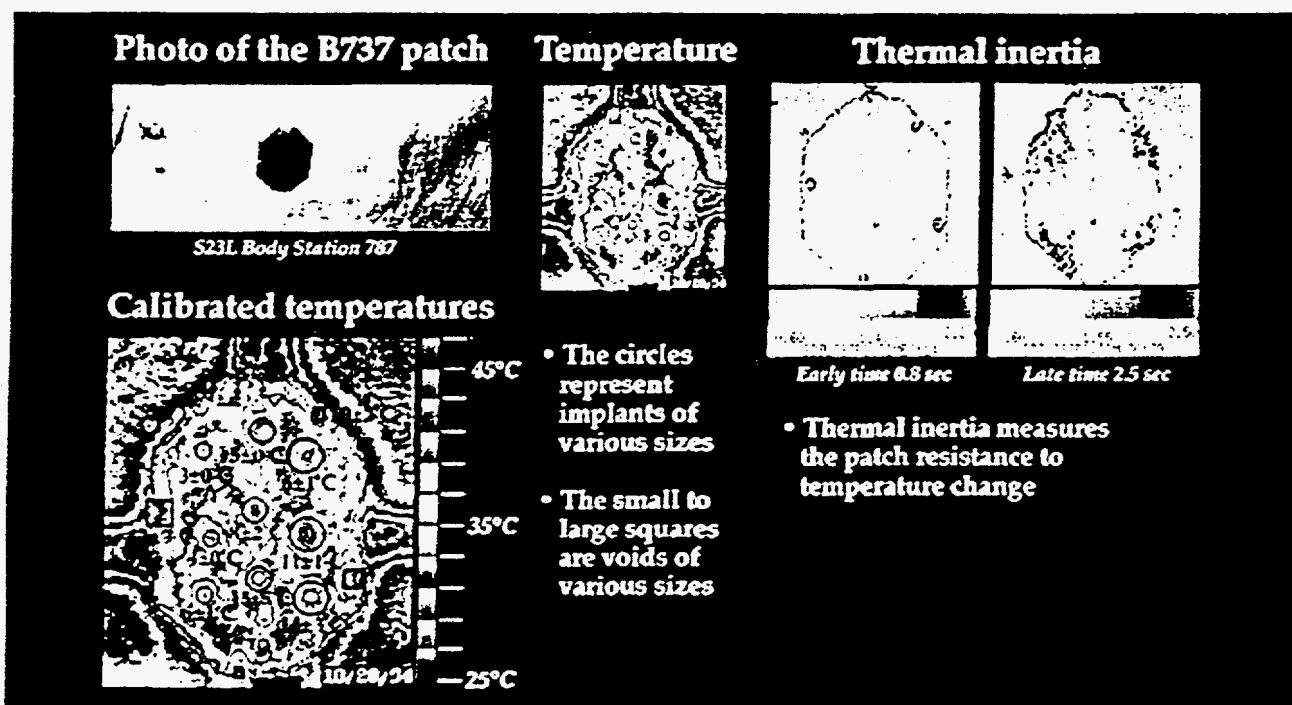
3.8 Imaging heat damage within a graphite-epoxy composite dome

We investigated heat damage at the upper rim center of a graphite epoxy dome seen at the left side of Figure 10. Two white (hot) lobes have temperatures above 70 °C as seen at 0.040 s after onset of the heat flash on the left and again (enlarged) at the upper left corner or four detailed pictures on the right side of Figure 10. The remaining three detailed pictures show changes in heat damage with depth inferred by dynamic changes in the relative thermal inertia of the heat-damaged zone. The heat damage was caused by applying heat from a hot-air gun during a prolonged period of time.

In the upper right corner of Figure 10 is an early-time thermal inertia map showing shallow-layer heat damage. This map was a reconstruction of the temperature-time history taken at early times from 0.2 s to 1.0 s after the heat flash. The black lobes have the least thermal inertia (resistance to temperature change) at heat-damaged sites which reached the hottest temperatures. At intermediate times (1 s to 3 s) the low (black) thermal inertia zone had a circular perimeter which enclosed both lobes and a smaller undamaged center (lower center). At late times (3 s to 8 s), the diameter of the heat-damaged zone decreased.



(A) Boeing 737 percent metal loss calibrations were made with a known reference standard. Infrared and ultra-sound methods agree qualitatively.



(B) Boron patch temperature maps measure flaw sizes and dynamic thermal inertia maps determine flaw types (implant, void, unbond) and depths.

Figure 7. Boeing 737 defects in (A) fuselage and (B) boron-epoxy doubler.

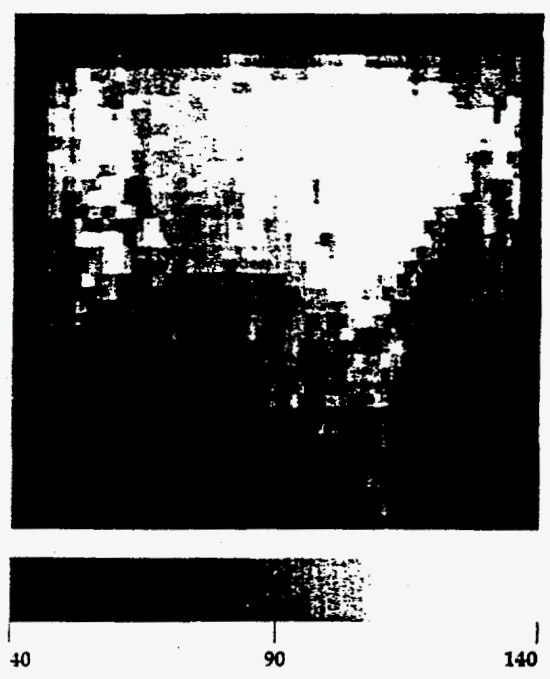
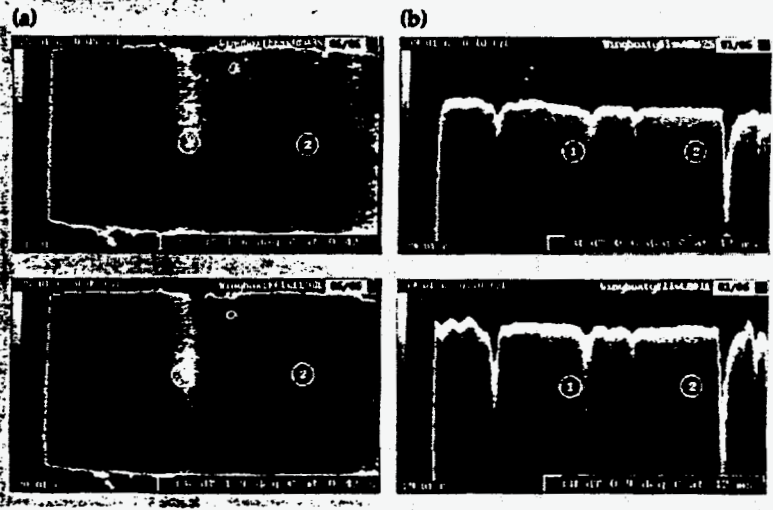


Figure 6.

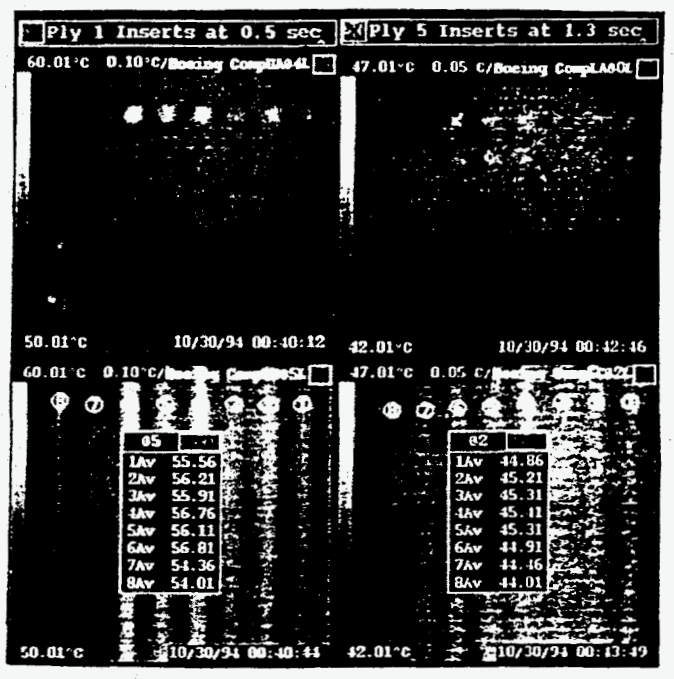
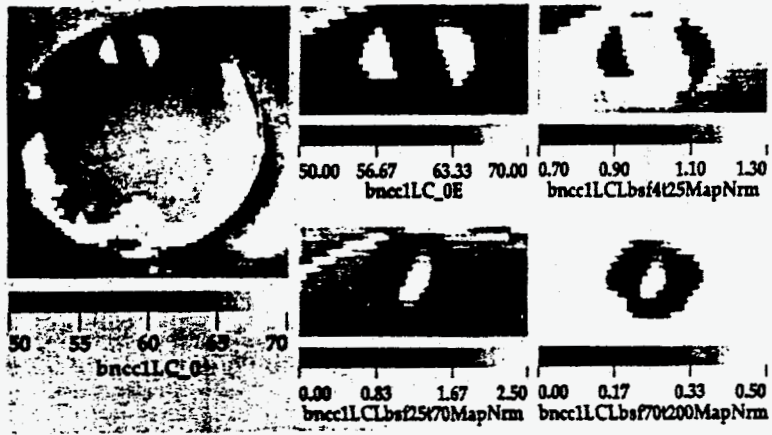


Figure 8.

Figure 9.

3.9 Composite structure with multiple inserts

We measured density, cooling rate and thermal inertia signatures for eight inserts at 1 ply (0.19 mm) and 5 ply (0.94 mm) depths in a composite panel from Boeing shown in Figure 11. Longwave (LW) pulsed-thermal images and linescan timegrams are respectively at the top and bottom of the figure. At the top of Figure 11, eight 0.5 inch square inserts, 1-ply deep (first row) are seen at 0.5 s after the flash (on the left) and inserts 1-ply and 5-ply deep (first and second rows) are seen at 1.3 s after the flash for the 5-ply-deep inserts (on the right).

4. ACKNOWLEDGMENTS

This work was performed by LLNL under the auspices of DOE contract number W-7405-ENG-48. We acknowledge support from the FAA Aging Aircraft Non-Destructive Inspection R&D Program, Interagency Agreement DTFA03-92-A-00007. We valued the use of the Bales uniform flashlamp source and hood, the Rockwell reference standards developed by Steve James, the F-15 wing box from Owen Manning at Northrop, the composite panel with inserts from Jeff Thompson at Boeing, the corroded KC-135 panel from ARINC, the corroded pipeline samples from Russell Mack at Dow Chemical and the ultra-sound image in Figure 7 from D. K. Hsu at Iowa State University. We acknowledge the VIEW code image processing macros developed by Dwight Perkins and Mike Gorvad, the figure layouts by Marsha Bell, the LLNL overall LLNL support of Ken Dolan, Satish Kulkarni and Harry Martz, and FAA/AANC Sandia NM support of Pat Walter, Craig Jones, and Ken Harmon.

5. REFERENCES

1. Spicer, J. W. M., W. D. Kerns, L. C. Aamodt, R. Osiander and J. C. Murphy, "Time-Resolved Infrared Radiometry (TRIR) using a Focalplane Array for Characterizations of Hidden Corrosion", Proceedings of SPIE Conference 1933: Thermosense XV, Ed. Lee R. Allen, Orlando FL p. 148, 1993.
2. Favro, L. D., P. K. Kuo, R. L. Thomas, T. Ahmed and Y. X. Wang, "Thermal wave imaging of corrosion and disbonds in aircraft structures" in Proceedings of SPIE Conference 2001: Nondestructive Inspection of Aging Aircraft, Ed. Michael T. Valley, Nancy K. Del Grande and Albert S. Kobayashi, San Diego CA, p. 88-91, July, 1993.
3. Selman, John J. and J. Ted Miller, "Evaluation of a prototype thermal wave imaging system for nondestructive evaluation of composite and aluminum aerospace structures", Proceedings of SPIE Conference 1933: Thermosense XV, Ed. Lee R. Allen, Orlando FL p. 178, 1993.
4. Syed, Hazari I., and K. Elliott Cramer, "Corrosion Detection in Aircraft Skin", Proceedings of SPIE Conference 1933: Thermosense XV, Ed. Lee R. Allen, Orlando FL, p. 160, 1993.
5. Vavilov, V. P. and X. Maldague, "Dynamic thermal tomography: a new promise in the IR thermography of solids", Proceedings of SPIE Conference 1682: Thermosense XIV, Ed. Jan K. Eklund, Orlando FL p. 194, 1992.
6. John Alcott, "An Investigation of Nondestructive Inspection of Nondestructive Inspection Equipment: Detecting Hidden Corrosion on USAF Aircraft" in Materials Evaluation, American Society for Nondestructive Testing, Jan., 1994.
7. N. K. Del Grande, K. W. Dolan, P. F. Durbin and D. E. Perkins, "Emissivity-Corrected Infrared Method for Imaging Anomalous Structural Heat Flows", Patent Release, RL-12164, March, 1995.
8. Nancy A. Del Grande, Philip F. Durbin and Michael R. Gorvad, "Infrared Computed Tomography" in Nondestructive Evaluation Thrust Area Report FY93, Engineering Research Development and Technology, Ed. Harry E. Martz, UCRL-ID-115668, May, 1994.
9. Nancy K. Del Grande and Philip F. Durbin, "Multi-use applications of dual-band infrared (DBIR) thermal imaging for detecting structural defects" in Proceedings of SPIE Conference 2217: Aerial Surveillance Sensing Including Obscured and Underground Object Detection, Ed. Ivan Cindrich, Nancy K. Del Grande, Sankaran Gowrinathan, Peter Johnson and James F. Shanley, Orlando FL, p. 107-116 Apr. 1994.
10. N. K. Del Grande and P. F. Durbin, "Dual-Band Infrared Imaging to Detect Corrosion Damage Within Airframes and Concrete Structures", in Proceedings of SPIE Thermosense XVI, International Conference on Thermal Sensing and Imaging and Diagnostic Applications, Ed. John Snell, Orlando FL, p. 202-209, Apr. 1994.

11. N. K. Del Grande, "Dual Band Infrared Imaging for Quantitative Corrosion Detection in Aging Aircraft", Proceedings of the American Society for Nondestructive Testing (ASNT) Meeting, Nov. 1993.
12. N. K. Del Grande, K. W. Dolan, P. F. Durbin, M. R. Gorvad and A. B. Shapiro, "Dual-Band Infrared (DBIR) Imaging Inspections of Boeing 737 and KC-135 Aircraft Panels", UCRL Report: Interagency Agreement DTFA03-92-A-0007 (1993). Original July, 1993. Revised November, 1993.
13. N. K. Del Grande, K. W. Dolan, P. F. Durbin, M. R. Gorvad and A. B. Shapiro, "Dynamic thermal tomography for nondestructive inspection of aging aircraft" in Proceedings of SPIE Conference 2001: Nondestructive Inspection of Aging Aircraft, Ed. Michael T. Valley, Nancy K. Del Grande and Albert S. Kobayashi, San Diego CA, p. 66-77, July 1993.
14. N. K. Del Grande, K. W. Dolan, P. F. Durbin, M. R. Gorvad, B. T. Komblum, D. E. Perkins, D. J. Schneberk and A. B. Shapiro, "Three-Dimensional Dynamic Thermal Imaging of Structural Flaws by Dual-band Infrared Computed Tomography" in Proceedings of SPIE Conference 1942: Underground and Obscured Object Imaging and Detection, Ed. Nancy Del Grande, Ivan Cindrich and Peter Johnson, Orlando FL, p. 207-215, Apr. 1993.
15. N. K. Del Grande, P. F. Durbin and D. E. Perkins, "Dual-Band Infrared Imaging Applications: Locating Buried Minefields, Mapping Sea Ice, And Inspecting Aging Aircraft", Review of Progress in Quantitative Nondestructive Evaluation, Ed. D. O. Thompson and D. E. Chimenti, Plenum Pr. NY, 12A, 465-472, 1993.
16. L. A. LeSchack and N. K. Del Grande, "A Dual-Wavelength Thermal Infrared Scanner As A Potential Airborne Geophysical Exploration Tool", see Appendix for derivation of Eq. (1) and Eq. (2), Geophysics 41, 1318, 1976.
17. John E. Lewis, Nancy Del Grande, Ian McKendry, Philip Durbin and Matti Lepparanta, "Thermal Mapping" in ERS-1 Baltic Sea Ice Calibration/Validation Post-Experiment Report / Pipor/Finland, Finnish Institute of Marine Research Report 1992 (9), Ed. Matti Lepparanta and Mikko Lensu, Helsinki, p. 55, 1992.
18. N. K. Del Grande, P. F. Durbin, M. R. Gorvad, D. E. Perkins, G. A. Clark, J. E. Hernandez and R. J. Sherwood, "Dual-band Infrared Capabilities for Imaging Buried Object Sites" in Proceedings of SPIE Conference 1942: Underground and Obscured Object Imaging and Detection, Ed. Nancy Del Grande, Ivan Cindrich and Peter Johnson, Orlando FL, 1993.
19. Nancy Del Grande, "Airborne Detection Of Buried Minefields", Energy and Technology Review, University of California LLNL Report, UCRL-52000-91-12, 1991.
20. N. K. Del Grande, G. A. Clark, P. F. Durbin, D. J. Fields, J. E. Hernandez and R. J. Sherwood, "Buried Object Remote Detection For Law Enforcement", Surveillance Technologies, SPIE Vol. 1479, 335, 1991.
21. N. K. Del Grande, "Airborne Temperature Survey Maps of Heat Flow Anomalies for Exploration Geology", Proceeding of International Symposium on Remote Sensing of Environment, Second Thematic Conference on Remote Sensing for Exploration Geology, Dec. 1982. Reprinted in Geothermal Resources Council Bulletin 14, p.3, Mar., 1985.
22. N. K. Del Grande, "Method for Identifying Anomalous Terrestrial Heat Flows"; Patent No. 4,005,289, 1977.
23. E. G. Grinzato, C. Bressan, P. G. Bison, A. Mazzoldi, P. Baggio, C. Bonacina, "Evaluation of moisture content in porous material by dynamic energy balance", Proceedings of SPIE Conference 1682: Thermosense XIV, Ed. Jan K. Eklund, Orlando FL p. 213, 1992.
24. Ph. M. Delpech, D. M. Boscher, F. Lepoutre, A. A. Deom and D. L. Balageas, "Quantitative nondestructive evaluation of carbon-carbon composites by pulsed infrared thermography", in Review of Progress in Quantitative Nondestructive Evaluation, 12B, Ed. by Donald O. Thompson and Dale E. Chimenti, Plenum Press, New York and London, p. 1297, 1993.
25. H. S. Carslaw and J. C. Jaeger, Conduction of Heat in Solids, 2nd Edition, Oxford Univ. Pr., London, pp. 101, 112 and 259, 1980.